J. Fluid Mech. (2023), *vol*. 966, A21, doi:10.1017/jfm.2023.432

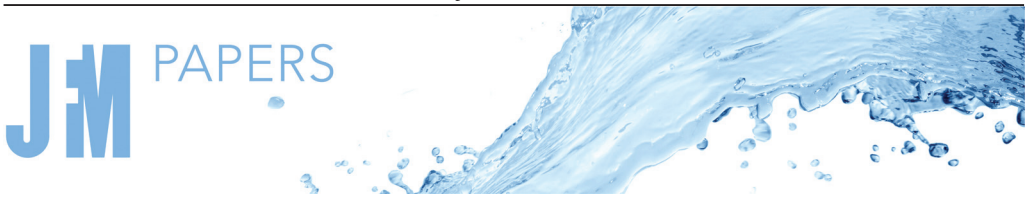

An experimental study of off-centred rotating thermal convection: a laboratory model for the tidal effects

Yun-Bing Hu[1,2] **and Ke-Qing Xia**[1,†]

[1]Center for Complex Flows and Soft Matter Research and Department of Mechanics and Aerospace Engineering, Southern University of Science and Technology, Shenzhen 518055, PR China

[2]Department of Physics, The Chinese University of Hong Kong, Shatin, Hong Kong, PR China

(Received 2 January 2023; revised 7 April 2023; accepted 22 May 2023)

A novel experiment was performed in rotating Rayleigh–Bénard convection (RRBC), wherein the convection cell with radius R was shifted away from the rotation axis by a distance d. In this case, the centrifugal force felt by a fluid parcel (characterized by the Froude number Fr) can be decomposed into an axisymmetrical part Fr_R and a directed one Fr_d. It has been reported that the global heat transport enhances at $Fr_{d,c}$ and then reaches an optimal state at $Fr_{d,max}$ (Hu *et al.*, *Phys. Rev. Lett.*, vol. 127, 2021, 244501). In this paper, the local properties after the offset effects set in are investigated further, which show different features before and after $Fr_{d,max}$. The local temperature measurements at the cell centre reveal that the bulk flow turns from a turbulent state into a laminar state at $Fr_{d,max}$, which is consistent with the particle image velocimetry results. This transition can be qualitatively understood by an equivalent tilted RRBC system. As for the hot and cold coherent structures near the sidewall, their vertical temperature variations reach a minimum at $Fr_{d,max}$, implying that these structures are mostly uniform in the vertical direction at $Fr_{d,max}$. Their temperature contrasts show a linear dependence on Fr_d and start to deviate from this linear behaviour when $Fr_d > Fr_{d,max}$. Besides the dominant effects of Fr_d, the secondary effects of Fr_R are also investigated. Due to the positive effect of $+Fr_R$ on the cold structure and the negative effect of $-Fr_R$ on the hot one, the cold structure is more coherent than the hot one, but its size is smaller. The shift of the cold cluster centre from the farthest point is also larger than the shift of the hot one from the nearest point.

Key words: Bénard convection, rotating flows

† Email address for correspondence: xiakq@sustech.edu.cn

1. Introduction

Rotating convective flows are of fundamental importance in many natural systems, such as in the atmospheres of planets and inside the stars. These geophysical and astrophysical systems are large in scale, complex in dynamics, and far from the reach in laboratory measurements. Nevertheless, the two most important factors in these systems, i.e. convection and rotation, have been explored over many years by a simplified model system – the rotating Rayleigh–Bénard convection (RRBC), where a rotating fluid layer is heated from below and cooled from above (Chandrasekhar 1981). In RRBC, convection is driven by the buoyancy force, which is caused by the applied temperature difference ΔT across the fluid layer. Its strength is characterized by the Rayleigh number $Ra = \alpha g \Delta T H^3/(\nu\kappa)$. Rotation introduces two effects in the system, i.e. the effects of the Coriolis force and the axisymmetrically distributed centrifugal force, which can be quantified by the Rossby number $Ro = U_{ff}/(2\Omega H)$ and the Froude number $Fr_R = \Omega^2 R/g$, respectively. Here, Ω is the rotation speed antiparallel to the gravity g and $U_{ff} = \sqrt{\alpha g \Delta T H}$ is the free-fall velocity. The flow domain is characterized by the depth H and radius R. α, ν and κ are the thermal expansion coefficient, the kinematic viscosity and the thermal diffusivity of the working fluid, respectively.

For Earth's parameters, the Froude number is of the order of 10^{-3}. Thus, the centrifugal effect is often neglected in RRBC, and the Coriolis effect has attracted much attention instead (see, e.g. the review articles by Stevens, Clercx & Lohse (2013), Kunnen (2021) and Ecke & Shishkina (2023)). The effects of the Coriolis force are twofold. In the bulk region of isothermal flows, the balance between the Coriolis force and the pressure gradient dominates the dynamics, i.e.

$$2\boldsymbol{\Omega} \times \boldsymbol{u} = -\nabla p \quad \xrightarrow{\nabla\times(\cdot)} \quad \partial_z \boldsymbol{u} = \boldsymbol{0}. \tag{1.1}$$

This so-called Taylor–Proudman (TP) constraint (Proudman 1916; Taylor 1923) makes the flow two-dimensional. However, in RRBC with temperature gradient, the TP constraint is replaced by the thermal wind balance, i.e.

$$2\boldsymbol{\Omega} \times \boldsymbol{u} = -\nabla p + \alpha g T \boldsymbol{e_z} \quad \xrightarrow{\nabla\times(\cdot)} \quad \partial_z \boldsymbol{u} = \frac{\alpha g}{2\Omega} \boldsymbol{e_z} \times \nabla T. \tag{1.2}$$

It can be seen that the effect of the temperature gradient is to violate the TP constraint and the resulting convective motion tends to make the flow three-dimensional-like (King *et al.* 2009; Grooms *et al.* 2010). The competition between the effects of the Coriolis force and the temperature gradient makes the RRBC system exhibit rich and complex flow phenomena (Sprague *et al.* 2006; Julien *et al.* 2012; Cheng *et al.* 2020). On the other hand, in the boundary layer, the effect of thermal wind balance is replaced by the Ekman pumping, which changes the flow dynamics there (Kunnen, Geurts & Clercx 2010; Kunnen *et al.* 2011*b*; Plumley *et al.* 2016) and enhances the vertical transport efficiency (Zhong *et al.* 2009; Stevens, Clercx & Lohse 2010; Weiss *et al.* 2010; Weiss, Wei & Ahlers 2016).

Recently, the centrifugal effect has also received some attention. The centrifugal force tends to generate accumulations of hot fluid parcels at the cell centre and cold ones around the sidewall. After the centrifugal effect sets in, the flow states can be divided into a weak- and a strong-centrifugal regime (Hu, Xie & Xia 2022). In the weak-centrifugal regime, the radial diffusive motions of hot and cold columns are enhanced (Noto *et al.* 2019; Ding *et al.* 2021); whereas in the strong-centrifugal regime, the columns are squeezed by the strong centrifugal force to form a large hot coherent structure at the cell centre (Horn & Aurnou 2018, 2019).

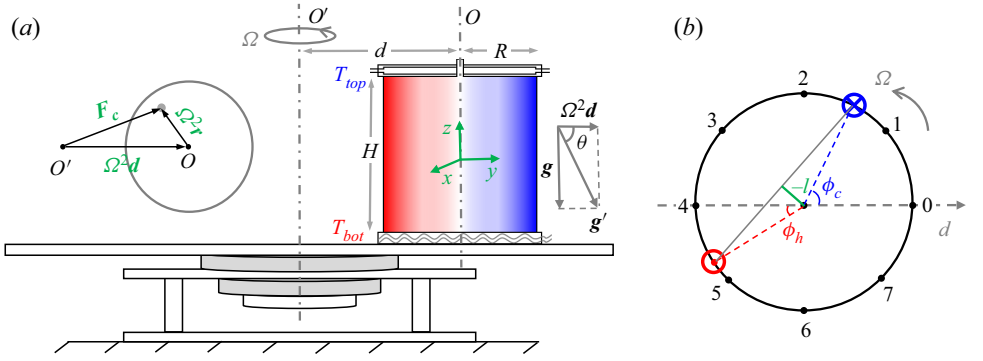

Figure 1. (*a*) A sketch of the off-centred experimental set-up. The convection cell is shifted away from the rotation axis with an offset distance d. The top view on the left-hand side shows that the centrifugal force $\boldsymbol{F}_c$ felt by a fluid parcel can be decomposed into an axisymmetrical part $\Omega^2\boldsymbol{r}$ and a directed one $\Omega^2\boldsymbol{d}$. (*b*) A sketch shows the azimuthal positions of the sidewall thermistors and the physical meanings of the quantities that obtained from the TEE method. The azimuthal positions of the coldest (ϕ_c) and hottest (ϕ_h) points are defined relative to the farthest ($\phi = 0$) and nearest ($\phi = \pi$) points, respectively. The vertical plane that defined by the coldest and hottest positions does not pass through the centre of the convection cell and shows an offset distance $-l$. See § 2.2 for further explanation.

In astronomy, a celestial body is often coupled with other planets or stars, such as the Earth–Moon system and the binary star systems. Therefore, besides the self-gravity g, the convective flows in a planet are often affected by an external gravity (i.e. the tidal force), which is exerted by the nearby planet or star. The most striking example in the solar system is Jupiter's moon, Io. The dramatic tidal force from Jupiter causes Io's solid surface to bulge up and down by many 10s of metres (Spencer & Schneider 1996). For comparison, the height of the tides in the Earth's ocean is only $O(10)$ m. This tidal force changes the dynamics of the partial-melt asthenosphere inside Io, and makes Io the most volcanically active world in the solar system (Hamilton *et al.* 2013; Steinke *et al.* 2020). Io is tidally locked to Jupiter. Thus, on Io's surface, there is always a nearest (the subjovian point) and a farthest (the antijovian point) point to Jupiter. The theories, which treat Io as essentially a solid body (Tyler, Henning & Hamilton 2015), predict that the volcanoes are most active near the subjovian and antijovian points (Segatz *et al.* 1988), which is in qualitative agreement with the observations. Unexpectedly, a detailed investigation of the global distribution of volcanoes on Io revealed a 30°–60° offset of the volcano cluster centres from the tidal axis (Hamilton *et al.* 2013; Steinke *et al.* 2020). This was partially explained by the assumption of the existence of a magma ocean inside Io, in which case the fluidity allows the Coriolis force to take effect (Tyler *et al.* 2015).

To model the tidal effects in the laboratory, we performed a novel experiment in RRBC, where the convection cell was shifted away from the rotation axis by an offset distance d (see figure 1*a*). With the rotating frame set at the cell centre, the centrifugal force that is felt by a fluid parcel can be decomposed into an axisymmetrical part $\Omega^2\boldsymbol{r}$ and a directed one $\Omega^2\boldsymbol{d}$. The later is characterized by a new Froude number $Fr_d = \Omega^2 d/g$. In a recent paper (Hu *et al.* 2021), it has been reported that the symmetry of the system is broken by this directed centrifugal force, resulting in a flow bifurcation. Specifically, the hot and cold fluid parcels are separated by $\Omega^2 d$ and condensed, respectively, near the nearest and farthest points to the rotation axis. Moreover, the condensation centres also show an offset from the nearest and farthest points. These behaviours are quite similar to the key features of the volcano distributions on Io described above, the reason of which is that this directed centrifugal force plays a role similar to the tidal force in Io.

The results in Hu *et al.* (2021) mainly concern the properties with and without the offset effects, namely, after the offset effects set in, the flow bifurcates and correspondingly, the global heat transport starts to enhance at an onset Froude number $Fr_{d,c}$ and then reaches an optimal state at $Fr_{d,max}$. Whereas the present work focuses on the local properties after the offset effects set in, showing different features before and after $Fr_{d,max}$. For example, the turbulent bulk flow, which is full of columns near onset, turns into a laminar state with 'empty' bulk at around $Fr_{d,max}$. This transition can be understood by an equivalent tilted RRBC system. On the other hand, the vertical temperature variations of the hot and cold coherent structures first decrease with Fr_d and then start to increase at $Fr_{d,max}$, implying that these structures are mostly uniform along the vertical direction at $Fr_{d,max}$. Their temperature contrasts, following a linear behaviour near onset, show a deviation from this linear dependence when $Fr_d > Fr_{d,max}$. Moreover, the effect of Fr_R has been investigated in the present study, which shows that the joint action of Fr_R and Fr_d results in a symmetry breaking in the centrifugal effect for the hot and cold fluid parcels; whereas only the effect of Fr_d was studied in Hu *et al.* (2021).

The remainder of this paper is organized as follows. The experimental set-up and the sidewall temperature analysis method are introduced in § 2. In the results section, we first briefly review the global features of this off-centred system in § 3.1, and then introduce the local properties of the bulk flow in § 3.2. As for the coherent structures in the sidewall region, their mean properties are first shown in § 3.3 and in the following section (§ 3.4), their local properties are investigated. Finally, we summarize our findings in § 4.

2. The experimental set-up and method

2.1. *The experimental set-up and parameters*

The structure of the rotating table has been described in detail in Hu *et al.* (2022). Here, only the key features and the differences with the centred experiments are introduced. The convection cell and all the other related equipment were seated on a large aluminium plate, whose diameter is 1500 mm. As sketched in figure 1(*a*), the convection cell was shifted away from the rotation axis with an offset distance d, which is normalized by the cell's radius $R = 97.1$ mm as $\gamma = d/R$. In order to change the offset distance d freely, a pair of sliding rails were used, above which the convection cell was seated. Seven different sets of experiments were performed, with the normalized value of $\gamma = 0.00$, 0.21, 0.82, 1.00, 1.65, 3.50 and 5.15. For $\gamma \leq 1.65$, the rotation speed changed from 6 r.p.m. to 60 r.p.m., resulting in the Rossby number Ro and the Froude number Fr_R covering the range of $0.045 \leq Ro \leq 0.44$ and $0.004 \leq Fr_R \leq 0.39$, respectively. For safety reasons, the rotation speed was only pushed to 52 r.p.m. (40 r.p.m.) for $\gamma = 3.50$ (5.15). Thus, the new Froude number Fr_d varied from 8×10^{-4} to 1.03.

This off-centred configuration not only makes the rotational inertia extremely large but also makes the whole rotational system unbalanced, which challenges the performance of our rotating table, especially for the case with large γ at large rotation speed. Thus, before the experiments, great care was taken to level the rotating table within 10^{-4} rad and to ensure system integrity. For safety reasons, the ramp-up speed of the table was set at 2 r.p.m. min^{-1} for each experiment. This extremely slow speed allows us to deal with any emergent events (if they happen). A weight balance was fixed at the opposite side of the sliding rails. If the mass of the balance was not enough, some noise, which was absent in the centred experiments, could be heard during the ramp-up process. This noise essentially arises from the residual imbalance of the system. In this case, the experiment was stopped

immediately and the mass of the balance was increased gradually. This procedure was repeated until the noise vanished, according to which we judged that the system was almost in balance. A Hall sensor and a camera were further used to monitor the working state of the rotating table.

The experimental set-up for heat transport measurements is similar to the one used in the standard Rayleigh–Bénard experiments. The cylindrical convection cell, which was filled with degassed and deionized water, has an aspect ratio $\Gamma = 2R/H = 1$ with its height $H =$ 194.2 mm. The heat flux q was applied to the hot bottom plate by heating nichrome wires, and then extracted by the cold top plate, whose temperature was regulated by a circulating water bath. In each plate, four thermistors were used to monitor their temperatures T_{bot} and T_{top}, respectively. During the experiments, the temperature difference $\Delta T = T_{bot} - T_{top}$ was kept at 16.0 K with an accuracy better than 0.1 K, resulting in a fixed Rayleigh number $Ra = 4.4 \times 10^9$. A small thermistor was used to measure the bulk temperature T_{bulk} at the cell centre. In the sidewall, 24 thermistors were distributed in three horizontal rows with altitudes $H/4$, $H/2$ and $3H/4$ from the bottom plate and in eight vertical columns equally spaced azimuthally. Their azimuthal positions $\phi_i = i\pi/4$ $(i = 0, 1, \ldots, 7)$ are defined in figure 1(*b*), with ϕ_0 corresponding to the farthest point to the rotation axis. All the thermistors used to measure temperatures were calibrated individually and separately in a temperature-controlled water bath, with a temperature accuracy better than 0.01 K. A copper basin was placed under the bottom plate to compensate the heat leakage from the bottom plate. Its temperature was regulated to $T_{bot} \pm 0.05$ K by a program. The convection cell was wrapped by several layers of Styrofoam to reduce the heat leakage from the sidewall, and then put into a home-made thermostat to minimize the influence of the fluctuating surrounding temperature. The temperature stability of the thermostat was better than 0.1 K. The Prandtl number $Pr = \nu/\kappa$ was fixed at 4.34, corresponding to 40.0 °C bulk temperature. The heat transport efficiency was quantified by the Nusselt number $Nu = q/(k\Delta T/H)$, with k the thermal conductivity of water.

The flow fields were visualized by particle image velocimetry (PIV) measurements (Xia, Sun & Zhou 2003; Sun, Xia & Tong 2005) for $\gamma = 0.00$, 0.82 and 3.50, and at each γ, $\Omega = 6$ r.p.m., 20 r.p.m., 27 r.p.m. and 40 r.p.m.. Another cylindrical cell, with radius $R = 96.8$ mm and height $H = 196.0$ mm, was used, outside which a rectangular jacket was fit to eliminate the optical distortion due to curvature of the sidewall. Limited by the space, two cylindrical lens were used to expand a 532 nm-laser into a lightsheet, whose thickness was around 3 mm. The measurement plane, defined by the rotation axis and the central axis of the cell, was illuminated by the lightsheet. The seeding particles were Dantec polyamid seeding particles with a diameter of 20 μm and a matched density of 1.03 g cm^{-3}. For each measurement, around 10 000 pictures were recorded with a frame rate of 20 Hz. To visualize the flow fields, the convection cell in PIV experiments cannot be well insulated. However, the jacket could isolate the flows from the surroundings, and the copper basin served to prevent heat leakage from below. It was found that for all PIV experiments, the measured Nusselt number was ∼5 % (max.) larger than that obtained in heat transport measurements. We believe that the heat leakage does not affect the observed flow phenomena significantly and thus the corresponding conclusions are not changed.

2.2. *Sidewall temperature analysis*

The nearly vertical single-roll large-scale circulation (LSC) in Rayleigh–Bénard convection gives rise to a sinusoidally shaped sidewall temperature profile. Thus, a sinusoidal-fitting method was usually adopted to study the dynamics of LSC (Brown,

Nikolaenko & Ahlers 2005; Brown & Ahlers 2006; Xi & Xia 2007). But this sinusoidal-fitting method has an obvious shortcoming, that is, it assumes the plane of the LSC must pass through the centre of the convection cell. With this constraint, the sloshing mode of LSC cannot be discovered until a new method, the temperature-extrema-extraction (TEE) method, was introduced (Xi *et al.* 2009; Zhou *et al.* 2009). In the off-centred RRBC, a similar sidewall temperature profile emerges owing to the condensation of the hot and cold coherent structures near the sidewall. As discussed in § 3.4, due to the asymmetry between these two coherent structures, the plane defined by the hottest and coldest positions does not pass through the cell centre. Therefore, the TEE method was adopted and extended here to study the properties of these coherent structures. The physical meanings of different quantities obtained from the TEE method are introduced below.

The TEE method was applied to the azimuthal temperature profiles measured at midheight only. At each moment t, find the coldest temperature and its two neighbours among the eight temperature signals. Then, by making a quadratic fitting $\tilde{T}(\phi, t) = a(t)\phi^2 + b(t)\phi + c(t)$, the minimum temperature $\tilde{T}_c(t) = (4ac - b^2)/4a$ at the position $\tilde{\phi}_c(t) = -b/2a$ can be obtained. Hereafter, a symbol with a tilde represents an instantaneous quantity. After time average, $\phi_c = \langle\tilde{\phi}_c\rangle_t$ and $T_c = \langle\tilde{T}_c\rangle_t$, the coldest position ϕ_c and the temperature contrast $\delta_c = (T_c - T_{bulk})/\Delta T$ can be defined to represent the condensation centre and the coherency of the cold coherent structure, respectively. We further define a new quantity $\beta_c = \langle 1/|a|\rangle_t/2\pi$. Mathematically, it is the length of the latus rectum of the quadratic curve. Physically, it represents the spatial spread range of the cold coherent structure along the azimuthal direction, or it implies how large the cold coherent structure is. The corresponding quantities for the hot coherent structure can be defined similarly. For convenience, the hottest position is defined relative to the nearest position, i.e. $\phi_h = \langle\tilde{\phi}_h\rangle_t - \pi$ (figure 1*b*). When $\phi_h \neq \phi_c$, the line that connects the hottest and coldest positions does not pass through the cell centre, resulting in an offset distance l (figure 1*b*). A simple calculation shows that l can be determined as $l = R\langle\sin((\tilde{\phi}_h - \tilde{\phi}_c)/2)\rangle_t$.

3. Results and discussions

3.1. *The global features of the off-centred RRBC*

The global features of the off-centred system have been studied in Hu *et al.* (2021). In this paper, this system is investigated further by local properties. For the sake of completeness, we first briefly review the global features here.

For the global heat transport in conventional RRBC (i.e. $d = 0$), a reduced Nusselt number $Nu_r = Nu/Nu(\Omega = 0)$ is defined to study the enhancement behaviour, which results from the effect of Ekman pumping. For the off-centred configuration, extra enhancement was observed. Therefore, another reduced Nu number $Nu_r^\gamma = Nu/Nu(\gamma = 0)$ is defined to single out the offset effects. Its behaviour has been discussed in detail in Hu *et al.* (2021) and two examples with $\gamma = 0.82$ and 3.50 are replotted in figure 2(*a*). Before the onset Froude number $Fr_{d,c} = 0.04$, Nu_r^γ is very close to unity. But for $Fr_d > Fr_{d,c}$, an enhancement of heat transport happens, from which an optimal state can be identified at $Fr_{d,max}$ (figure 2*a*). In this paper, the regimes with $Fr_{d,c} < Fr_d < Fr_{d,max}$ and $Fr_{d,max} < Fr_d$ are referred to as weak-Fr_d and strong-Fr_d regimes, respectively, and the local properties in each regime are investigated. It is further found that $Fr_{d,max}$ depends on γ as $Fr_{d,max} = 0.22\gamma^{0.47\pm0.02}$, but $Fr_{d,c}$ has a constant value of 0.04 (figure 2*b*).

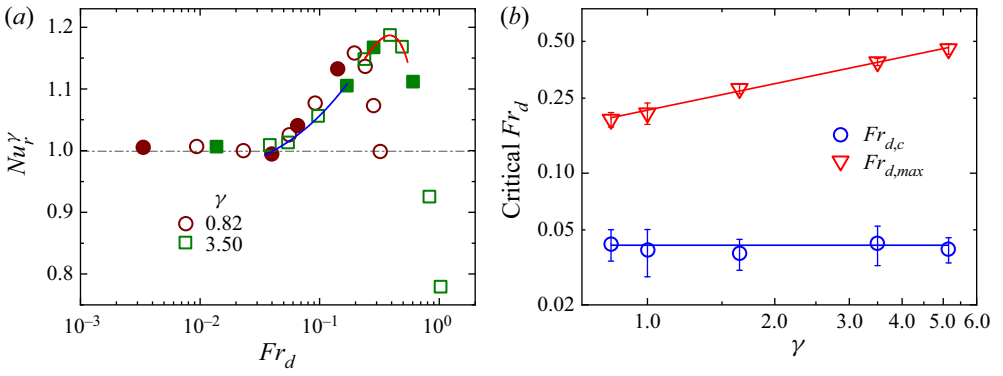

Figure 2. (*a*) The reduced Nusselt number Nu_r^γ as a function of Fr_d for $\gamma = 0.82$ and 3.50. The onset ($Fr_{d,c}$) and optimal ($Fr_{d,max}$) Froude numbers are defined, respectively, as the intersection of a logarithmic fitting (blue solid line) and the baseline $Nu_r^\gamma = 1.0$ and the peak of a parabolic fitting (red solid line). To relate the heat transport enhancement to the changes of flow fields in figure 3 conveniently, the cases that PIV measurements were also performed are indicated here by solid symbols. (*b*) The onset and optimal Froude numbers as a function of γ. The blue solid line indicates the mean value of the onset Froude number $Fr_{d,c} = 0.04$. The red solid line is a power-law fitting, $Fr_{d,max} = 0.22\gamma^{0.47\pm0.02}$. The error bars are the fitting errors.

The behaviour for $Fr_{d,max}$ can be explained successfully by two competing effects on heat transport (Hu *et al.* 2021), which will be discussed more completely in § 3.3. As for the onset Froude number $Fr_{d,c} = 0.04$, it has been argued that this value can be applied to the centred case (Hu *et al.* 2021). This is verified by a direct measurement in a recent RRBC experiment, which further shows that the onset value depends on Ra as $Ra^{0.53\pm0.04}$ (Hu *et al.* 2022). Here, it is worth pointing out that the onset Froude number $Fr_{d,c}$ may have important implications for the conventional RRBC experiments. During the experiments, the installation precision of the convection cell must be kept less than $d_c = gFr_{d,c}/\Omega^2$. (For example, for a fast rotation speed $\Omega = 2$ Hz and $Ra = 4.4 \times 10^9$, d_c is 2.5 mm.) Otherwise, the off-centre effects will set in to contaminate the results.

The global features of the flow fields are displayed in figure 3. For the reference case with $\gamma = 0.00$, because of the stronger TP effect at larger rotation speed, the suppression of vertical motion is more severe and the columns become more vertically uniform and horizontally confined. But for $\gamma > 0$, say $\gamma = 3.50$, different behaviour can be observed. The flow field bifurcates at large rotation speed. It can be seen that a hot and a cold coherent structures emerge near the sidewall, and their strength increases with increasing rotation speed, meanwhile the bulk region becomes more and more 'quiet'. Similar behaviours can be observed at fixed rotation speed but with increasing γ (e.g. figure 3*g–i*). This implies the importance of $Fr_d = \Omega^2 d/g$, which incorporates both Ω and γ. Close examination reveals that the heat transport enhancement at $Fr_d > 0.04$ in figure 2(*a*) (solid symbols) is closely related to the bifurcated flow states in figure 3. The flow fields, comparing the flow states with (i.e. $\gamma = 3.50$) and without (i.e. $\gamma = 0$) offset effects, have been shown in Hu *et al.* (2021). In this paper, the flow fields with $\gamma = 0.82$ are complemented to indicate the changes of the flow structures at weak- and strong-Fr_d regimes (see § 3.2 below). The bifurcated flow fields in figure 3 further show that the cold structure is always stronger than the hot one. The hot structure in figure 3(*h*) is so weak that it is intruded by cold flows. This asymmetry between the hot and cold structures are actually caused by the effect of $Fr_R = \Omega^2 R/g$, which will be discussed in detail in § 3.4 below.

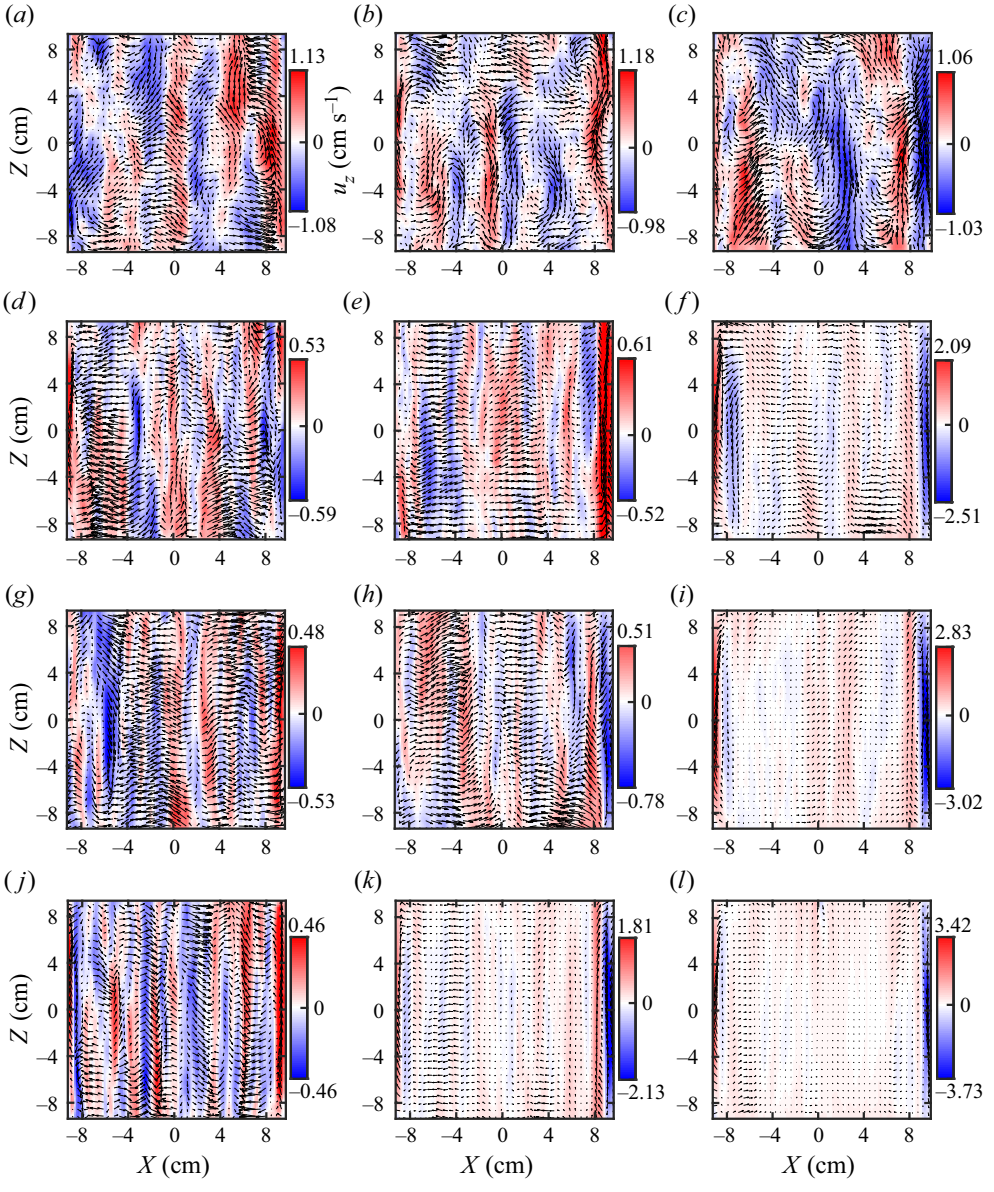

Figure 3. Time-averaged velocity fields for $\gamma = 0.00$ (*a*,*d*,*g*,*j*), 0.82 (*b*,*e*,*h*,*k*) and 3.50 (*c*,*f*,*i*,*l*), and for each γ, $\Omega = 6$ r.p.m., 20 r.p.m., 27 r.p.m. and 40 r.p.m. (from (*a–c*) to (*j–l*)). The corresponding parameters $[1/Ro, Fr_d]$ for each map are (*a*) [2.28, 0]; (*b*) [2.28, 0.003]; (*c*) [2.28, 0.01]; (*d*) [7.62,0]; (*e*) [7.59, 0.04]; (*f*) [7.57, 0.15]; (*g*) [10.23, 0]; (*h*) [10.21, 0.07]; (*i*) [10.17, 0.28]; (*j*) [15.19, 0]; (*k*) [15.25, 0.14]; (*l*) [15.11, 0.61]. The colour bars are coded by the vertical velocity u_z in unit of cm s^{-1} with the maximum and minimum values indicated in the respective maps.

3.2. *The properties of the bulk flow*

The mean flow fields in figure 3 suggest that, as Fr_d increases, the bulk flow becomes more and more 'quiet'. It seems that there exist two different flow states. At small Fr_d near $Fr_{d,c}$, the bulk region is still full of hot and cold columns (figure 3*h*), but at large Fr_d case, the bulk region is 'empty' (figure 3*l*). These two flow states can be seen more

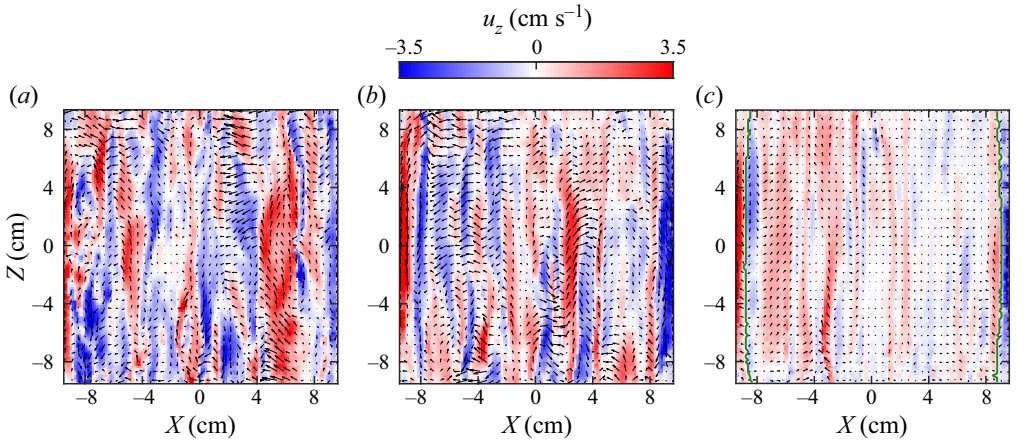

Figure 4. Instantaneous flow fields for $\gamma = 3.50$, (*a*) $\Omega = 20$ r.p.m., (*b*) 27 r.p.m. and (*c*) 40 r.p.m.. All three figures share the same colour bar. The dark green solid lines in (*c*) indicate the edges of the hot and cold coherent structures near the sidewall.

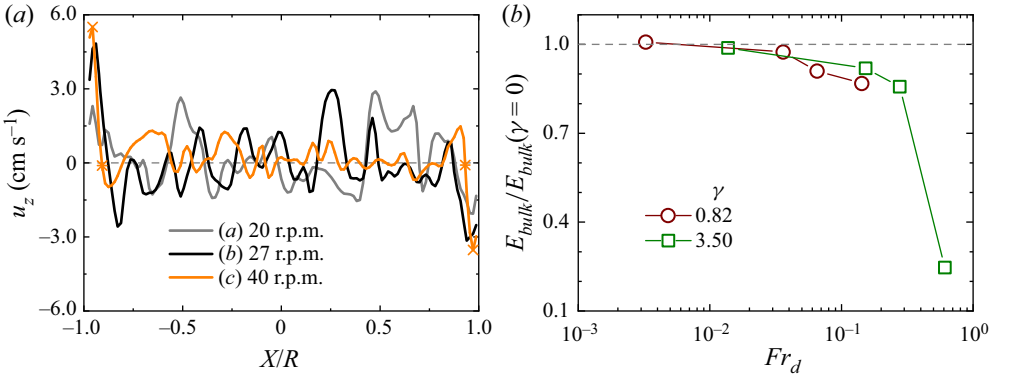

Figure 5. (*a*) Instantaneous horizontal profiles of u_z measured at midheight $Z = 0$ cm. These profiles are obtained from the measured instantaneous fields such as those shown in figure 4. (*b*) The mean kinetic energy E_{bulk} of the flow in the bulk region $X \in [-4\,\text{cm}, 4\,\text{cm}]$, which is normalized by the reference case $\gamma = 0$.

clearly in the instantaneous flow fields. Figure 4 displays the examples of the instantaneous flow fields for $\gamma = 3.50$. Compared with the corresponding mean flow fields in figure 3, the instantaneous bulk flow is much stronger. Figure 5(*a*) plots the horizontal profiles of $u_z(X)$, which are calculated from the instantaneous fields shown in figure 4 at $Z = 0$ cm. For small $Fr_d = 0.15$ (figure 4*a*), the field is full of hot and cold columns. Based on the velocity time series from the PIV measurements, we found that for most of the time, the flow near the left-hand (right-hand) sidewall region is always hot (cold) but with large fluctuations, suggesting that the hot (cold) coherent structure has already emerged near the sidewall but with weak strength. As can be seen from figure 5(*a*), their strength is similar to the bulk columns (the grey solid line). The situation for the bulk flow at $Fr_d = 0.28$ (figure 4*b*) is similar, but the coherent structures are much stronger. The corresponding velocity profile in figure 5(*a*) (the black solid line) clearly shows that these two coherent structures near the sidewall are now sufficiently strong to distinguish themselves from the bulk columns. However, it becomes different for even larger $Fr_d = 0.61 (> Fr_{d,max})$ shown

in figure 4(*c*). The bulk region becomes quite 'empty' while the coherent structures near the sidewall are stronger. The orange solid line in figure 5(*a*) also implies that the bulk flow is weaker when compared with other cases.

One may argue that the weakened bulk flow observed in figure 4(*c*) may be caused by the stronger TP effects. In figure 5(*b*) the mean bulk kinetic energy E_{bulk} is plotted relative to the reference case to avoid the TP effects. The mean bulk kinetic energy is calculated as $E_{bulk} = \langle \int_{S_{bulk}} (\tilde{u}_x^2 + \tilde{u}_z^2)\, \mathrm{d}x\, \mathrm{d}z \rangle_t / 2$. Here, S_{bulk} is the bulk region covered by $-0.41 \leq X/R \leq 0.41$. Its value reflects the strength of the mean bulk flow. It can be seen that the strength of this mean flow decreases with increasing Fr_d. At small Fr_d, the strength of the bulk flow is close to the reference case. But at the largest Fr_d, it drops sharply. This behaviour, together with the instantaneous flow fields in figure 4, shows that there exist two flow states. At small Fr_d, the bulk region is full of columns, but at large Fr_d, the bulk is 'empty'. All these results imply the following physical picture.

Before the offset effects set in ($Fr_d < Fr_{d,c}$), the flow state is similar to the centred case. The bulk region is full of hot and cold columns, which have a random-walk-like diffusive horizontal motion (Noto *et al.* 2019; Chong *et al.* 2020). When the directed centrifugal force starts to manifest itself ($Fr_d \gtrsim Fr_{d,c}$), the column's diffusive motion is modified by this weak directed force. Just like the centred case with very weak centrifugal force (Noto *et al.* 2019), the horizontal motion still has diffusive behaviour at small time scale, since the bulk region is full of columns. But at large time scale, the columns show directed motion. They meander to the sidewall gradually and accumulate there. However, due to the strong directed centrifugal force at very large Fr_d, they migrate to the sidewall quickly and merge with others there, leaving a relatively empty bulk region.

To more systematically study the flow dynamics in the bulk region, we turn to the local temperature signals, which are measured by a small thermistor placed at the cell centre. For the reference case $\gamma = 0.00$, we find that the r.m.s. value of the bulk temperature $T_{rms} = \sqrt{\langle (\tilde{T} - \langle \tilde{T} \rangle_t)^2 \rangle_t}$ follows a power-law scaling, i.e. $T_{rms}/\Delta T = 0.016 Ro^{-0.23\pm0.01}$, which is consistent with the finding from a previous study at $Ra = 4.5 \times 10^9$ (Hu *et al.* 2022). With this baseline, we can define $T_{rms}/T_{rms}(\gamma = 0)$ to study the offset effects, as shown in figure 6(*a*). The inset in figure 6(*a*) is an enlarged view of the data near $T_{rms}/T_{rms}(\gamma = 0) = 1$. It can be seen that for all γ, $T_{rms}/T_{rms}(\gamma = 0) > 1$ as soon as $Fr_d \gtrsim Fr_{d,c}^* = 0.02$, suggesting that the bulk flow becomes more turbulent as compared with the centred case. This is because, after the effects of the directed centrifugal force set in, the horizontal motion of the hot and cold columns in the bulk region are enhanced. Note that $Fr_{d,c}^* = 0.02$ is smaller than the value obtained from the global measurement, $Fr_{d,c} = 0.04$. This is because the local measurement is more sensitive to the changes of the flow dynamics than the global measurement. This has been discussed in Hu *et al.* (2021), in which a smaller value of onset Froude number 0.012 was obtained from the local sidewall temperature measurement. At larger Fr_d, T_{rms} becomes smaller than the reference value $T_{rms}(\gamma = 0)$ and decreases quickly thereafter, which can be attributed to the columns moving out of the bulk region, as suggested by the PIV result. Again, due to the sensitivity of the local measurement, the value of Fr_d, where $T_{rms}/T_{rms}(\gamma = 0)$ starts to decrease below unity, is smaller than $Fr_{d,max}$. But as a rough estimation, we can conclude that this happens at around $Fr_{d,max}$.

The power spectral density (PSD) suggests a similar physical picture. An example for $\gamma = 3.50$ is shown in figure 6(*b*), which is calculated based on the normalized temperature signal $(\tilde{T} - \langle \tilde{T} \rangle_t)/T_{rms}$ at the cell centre. These PSDs can be divided into two groups. One is for the cases with $Fr_d < Fr_{d,max} = 0.39$, which nearly collapse on top of each other

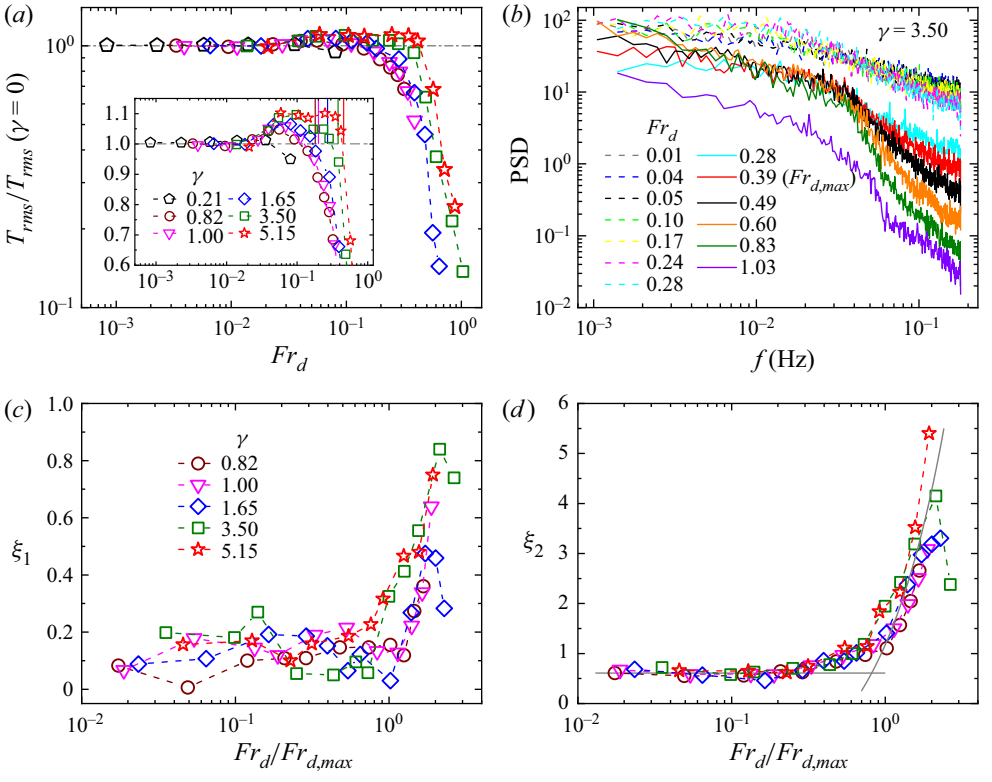

Figure 6. (*a*) The root-mean-square (r.m.s.) of bulk temperature T_{rms} normalized by the reference case $T_{rms}(\gamma = 0)$. Inset is an enlarged view to show the increased fluctuations more clearly. The short vertical solid lines indicate the values of $Fr_{d,max}$ obtained from the Nu data for each γ. (*b*) The power spectral density (PSD) of $(T - \langle T\rangle_t)/T_{rms}$ for $\gamma = 3.50$. For clarity, the cases with dash lines are shifted up by $10^{0.6}$. Panels (*c*,*d*) plot the roll-off rates ξ_1 and ξ_2 at small and large f, respectively. The horizontal grey solid line in (*d*) is the mean value 0.61 of ξ_2 with $Fr_d/Fr_{d,max} < 0.2$. The other grey solid line is a linear fitting $\xi_2 = 3.1Fr_d/Fr_{d,max} - 1.9$ to the data within $1 < Fr_d/Fr_{d,max} < 2$.

(they are shifted up by $10^{0.6}$ for clarity in figure 6*b*). The bulk flow for these cases is still turbulent, and broad scales of motion can be excited. Thus, the roll-off of the PSD is slow. However, as soon as $Fr_d > 0.39$, the PSD drops quickly at large f to approach the cut-off frequency, since for these cases the flow becomes increasingly laminar. The same behaviours can be found for other γ. It can be seen from figure 6(*b*) that for each case, the roll-off rate at small f is slower than the one at large f. For the cases with $Fr_d < 0.39$, the transition of the roll-off rate happens at around 0.015 Hz. But it is around 0.035 Hz when $Fr_d > 0.39$. Power laws, $f^{-\xi_1}$ and $f^{-\xi_2}$, are used to describe the roll-off before and after the transition frequency, respectively. The roll-off rates ξ_1 and ξ_2 are shown as a function of $Fr_d/Fr_{d,max}$ in figures 6(*c*) and 6(*d*), respectively. The result of ξ_1 is much more scattered than that of ξ_2, since there are much fewer PSD data points to be fitted at small f. But the transition in ξ_1 at around $Fr_d/Fr_{d,max} = 1$ is quite clear (figure 6*c*). The results of ξ_2 for different γ are collapsed together (figure 6*d*). It can be seen that there is a plateau $\xi_2 = 0.61$ at small $Fr_d/Fr_{d,max}$, but after some critical value, ξ_2 starts to increase. Note that this behaviour is quite similar to the one of the mean temperature profile in Rayleigh–Bénard convection, in which case the thermal boundary layer thickness is defined to be the intersection of a linear fitting and a constant value (Ahlers, Grossmann

& Lohse 2009; Zhou & Xia 2013). Therefore, this slope method is also adopted here to find the critical value in ξ_2. The increment at large $Fr_d/Fr_{d,max}$ can be roughly described by a linear function $\xi_2 = 3.1Fr_d/Fr_{d,max} - 1.9$, which intersects with the baseline $\xi_2 = 0.61$ at $Fr_d/Fr_{d,max} = 0.82$. The value $Fr_d/Fr_{d,max} = 0.82$, which is close to unity, implies that ξ_2 starts to increase quickly at around $Fr_{d,max}$. This is consistent with the PSD behaviours observed in figure 6(*b*).

It is clear from the above that in this off-centred system, two flow states exist and the transition between them happens at around $Fr_{d,max}$, roughly consistent with the regime division by the optimal heat transport state at $Fr_{d,max}$. Therefore, we can conclude that in the weak-Fr_d regime with $Fr_d < Fr_{d,max}$, the emerged hot and cold coherent structures near the sidewall are not so strong and the bulk is still full of hot and cold columns whose motion along the direction of d is enhanced by Fr_d. But in the strong-Fr_d regime with $Fr_d > Fr_{d,max}$, the coherent structures near the sidewall are much stronger and the bulk region becomes relatively 'empty'. The emergence of these two different flow states can be understood qualitatively as follows.

The directed centrifugal force $\Omega^2\boldsymbol{d}$ can be regarded as a type of gravity, and then we can define an effective gravity as $\boldsymbol{g'} = \boldsymbol{g} + \Omega^2\boldsymbol{d}$ with a tilted angle θ relative to the horizontal plane (figure 1*a*). With this effective gravity $\boldsymbol{g'}$, the off-centred RRBC system is equivalent to a centred one, but with a misalignment between the rotation axis and the gravity $\boldsymbol{g'}$. This tilted system (von Hardenberg *et al.* 2015; Novi *et al.* 2019; Zhang, Ding & Xia 2021) can be regarded as an extension of the conventional RRBC system. Depending on the value of the tilted angle θ, there exist two different flow states, which we shall refer to as the 'column state' and the 'sheared wind state'. For $\theta = 90^\circ$, the conventional RRBC is recovered, which is full of columns and mimics the flows near the polar regions of a planet. But for $\theta = 0^\circ$, a new state with sheared, intermittent large-scale winds emerges (von Hardenberg *et al.* 2015), which models the zonal flows near the equatorial region. With increasing values of θ, a transition from the 'sheared wind state' to the 'column state' occurs at $\theta = 45^\circ$–60° (Novi *et al.* 2019). Note that $1/Fr_d = \tan\theta$. Thus, at small Fr_d (large θ), the flow state of the off-centred system in the weak-Fr_d regime is just like the 'column state' of the tilted RRBC system. As for large Fr_d (small θ), the hot and cold coherent structures near the sidewall resemble the winds in the 'sheared wind state'. It has been shown that the flow directions of the sheared winds are perpendicular to the plane defined by the gravity and rotation vectors, and form a cyclonic flow (von Hardenberg *et al.* 2015). Thus, the hot and cold structures will deflect cyclonically, as shown by the behaviors of the cluster centres ϕ_h and ϕ_c in § 3.4. The interplay among the 'winds', the Coriolis force and the directed centrifugal force in the off-centred RRBC has been discussed in Hu *et al.* (2021).

3.3. *The coherent structures: mean properties*

In the following two sections, the properties of the hot and cold coherent structures near the sidewall are investigated. We first discuss their mean properties here. Figure 5(*a*) shows an example (the orange solid line) of how these coherent structures are identified from the PIV measurements. At each height, one finds the first maximum (minimum) vertical velocity u_z from the left-hand (right-hand) side (the crosses), and next search for the nearest position with a minimum $|u_z|$ (the stars), which is identified as the edge of the hot (cold) coherent structure at this height. The so-obtained edges of these coherent structures are indicated by dark green solid lines in figure 4(*c*). Once these coherent structures are identified, their mean velocity can be obtained as $U = \langle(\tilde{u}_x^2 + \tilde{u}_z^2)^{1/2}\rangle_{S_{h+c},t}$. Here, $\langle\cdot\rangle_{S_{h+c},t}$ means average over the total area of the hot and cold coherent structures S_{h+c} and the

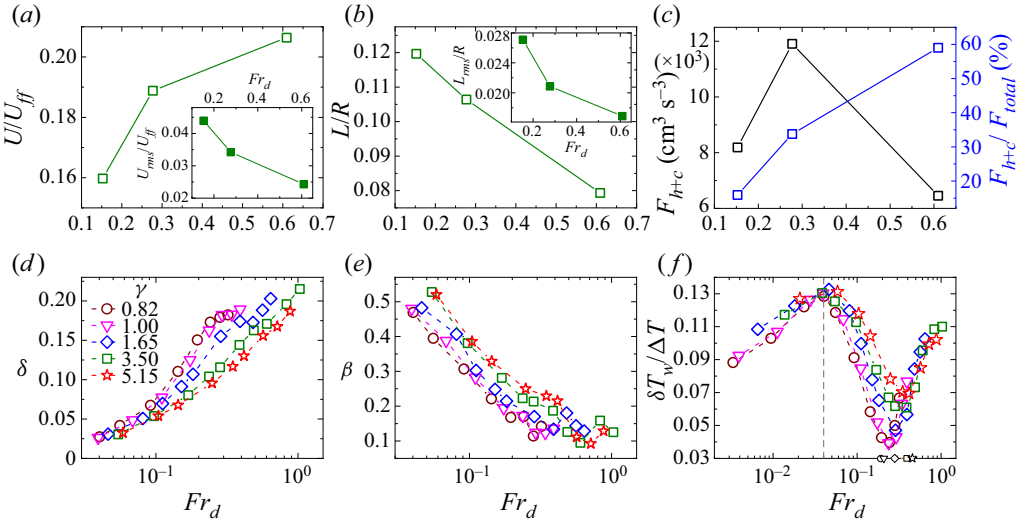

Figure 7. (*a*) The mean velocity U, (*b*) mean width L and (*c*) the kinetic energy flux F_{h+c} of the coherent structures obtained from PIV measurements for $\gamma = 3.50$. Here U and L are normalized by the free-fall velocity U_{ff} and the radius of the cell R, respectively. The insets in (*a*,*b*) are the corresponding r.m.s. values. The blue open squares in (*c*) indicate how much the coherent structures contribute to the flux of the whole flow field. (*d*) The mean temperature contrast δ and (*e*) mean distribution range β obtained from the TEE method. (*f*) The sidewall temperature variation δT_w normalized by ΔT. The vertical dash line is $Fr_{d,c} = 0.04$, and the black open symbols in the x-axis are the $Fr_{d,max}$ for each γ. The data have been shifted vertically to show $Fr_{d,c}$ more clearly.

time t. The mean width L of the coherent structures can be defined similarly. The results for $\gamma = 3.50$ are shown in figures 7(*a*) and 7(*b*), respectively. It can be seen that the velocity U of the coherent structures increases with Fr_d, but the width L decreases. However, their r.m.s. values are both decreased (the insets in figure 7*a*,*b*), indicating that these coherent structures become more stable at larger Fr_d.

As it is impractical to study the long-term properties of the hot and cold coherent structures systematically using PIV measurements, we turn to the azimuthal temperature profiles measured at the sidewall. Figure 7(*d*,*e*) display the increased mean temperature contrast $\delta = (\delta_h + |\delta_c|)/2$ and the decreased mean distribution range $\beta = (\beta_h + \beta_c)/2$, respectively, which are obtained from the TEE method (see § 2.2) and are consistent with the PIV results shown above. These results, which only discuss the temperature contrast δ of the coherent structures and their dimension along the azimuthal direction β, have been discussed briefly in Hu *et al.* (2021). Here, together with the PIV results, a more complete physical picture can be obtained. As Fr_d increases, the hot and cold coherent structures are squeezed more severely by the directed centrifugal force. Thus, the dimensions along the radial (i.e. L) and azimuthal (i.e. β) directions are both decreased. On the other hand, this squeezing process is accompanied by a condensation of the heat content of the fluids. Thus, the temperature contrast δ of the coherent structures increases, which would result in a larger buoyancy force and then a larger velocity U. As shown below, the decreased size (i.e. the cross-section area $\sim L \times \beta$) and the increased coherency (i.e. $\sim \delta \times U$) are two competing effects for the heat transport.

Figure 7(*c*) plots the vertical flux of the kinetic energy of the coherent structures for $\gamma = 3.50$, which is defined as $F_{h+c} = \langle \int_{S_{h+c}} \tilde{E}\tilde{u}_z \, \mathrm{d}x \, \mathrm{d}z \rangle_t$. Here, $\tilde{E} = (\tilde{u}_x^2 + \tilde{u}_z^2)/2$. The behaviour exhibits an optimal flux state, which reminds us of the heat transport in figure 2(*a*). This is because from its definition, the increased velocity U of the coherent structures

competes with their decreased occupation area S_{h+c}. This implies that the decreased size and the increased coherency of the coherent structures are two competing effects for the heat transport. This can be seen more clearly from the definition of the Nu number, $Nu = \sqrt{RaPr}\langle u_z' T'\rangle_A$, where the contribution from conduction is neglected. Here, u_z' is the vertical velocity normalized by U_{ff}, $T' = (T - T_{bulk})/\Delta T$ and $\langle\cdot\rangle_A$ means average over the cross-section area of the cell $A = \pi R^2$. The open blue squares in figure 7(*c*) imply that the vertical transport is more and more dominated by the coherent structures near the sidewall. Thus, Nu can be estimated as $Nu = \sqrt{RaPr}\langle u_z' T'\rangle_A \sim \sqrt{RaPr}(A_{h+c}/A)\langle u_z' T'\rangle_{A_{h+c}}$, where A_{h+c} is the cross-section area of the hot and cold coherent structures. Now, it is straightforward that the decreased size A_{h+c}/A has a negative effect for heat transport, but the increased temperature contrast T' has a positive one. (Note that u_z' increases with T' because of the larger buoyancy force.) Indeed, it has been shown that the optimal heat transport state at $Fr_{d,max}$ can be explained successfully by these two competing effects (Hu *et al.* 2021).

The quantity $\delta T_w = 2\langle T_w^b - T_w^t\rangle_{\phi,t}$ in figure 7(*f*) characterizes the mean vertical temperature gradient near the sidewall, where $\langle T_w^b\rangle_{\phi,t}$ and $\langle T_w^t\rangle_{\phi,t}$ are the azimuthally and temporally averaged sidewall temperatures measured, respectively, at $H/4$ (bottom) and $3H/4$ (top). It has been reported that when there is no centrifugal effect, δT_w increases with rotation speed (Zhong & Ahlers 2010), which was then explained by the effects of the secondary flows in the Stewartson boundary layers near the sidewall (Kunnen *et al.* 2011*a*). At small $Fr_d < Fr_{d,c} = 0.04$, the offset effect does not set in and the increasing behaviour of δT_w in figure 7(*f*) is consistent with previous study (Zhong & Ahlers 2010). However, δT_w starts to drop at $Fr_{d,c} = 0.04$ for all γ, since the hot and cold coherent structures emerge near the sidewall and then the sidewall temperature becomes uniform at vertical direction. The drop at $Fr_{d,c} = 0.04$ is an implication that the dynamics of the sidewall boundary flows are changed and the Stewartson boundary layers are most likely to be replaced by these coherent structures. What is more interesting is that δT_w reaches a minimum at around $Fr_{d,max}$ for all γ. This implies that at the optimal transport state, the hot and cold coherent structures are most uniform along the vertical direction.

3.4. *The coherent structures: local properties and the secondary effects of Fr_R*

The local properties of the hot and cold coherent structures are presented in this section. It is found that the properties of these two types of structures are quite different. In the off-centred RRBC, the centrifugal force felt by a fluid parcel can be decomposed into an axisymmetrical part $Fr_R = \Omega^2 R/g$ and a directed one $Fr_d = \Omega^2 d/g$. It has previously been shown that the global features of the system are dominated by Fr_d (Hu *et al.* 2021). However, for the local properties, in addition to Fr_d, Fr_R also plays a role. As sketched in figure 8(*a*), the effect of the axisymmetrical centrifugal force Fr_R is to generate accumulations of the hot fluid parcels at the cell centre and the cold ones near the sidewall, and Fr_d tends to separate the hot and cold fluid parcels and condense them near the nearest and farthest points, respectively. As a result, the combined effect of these two forces is very different for the hot and cold fluid parcels. While these two forces cooperate to push the cold fluid parcels to the right-hand side, they compete with each other for hot ones. Broadly speaking, the total centrifugal forces experienced by the hot and cold fluid parcels are $Fr_d - Fr_R$ and $Fr_d + Fr_R$, respectively, and their difference is of the order of $2Fr_R$. The effects of Fr_R are important for the understanding of the discovered asymmetrical properties between the hot and cold coherent structures.

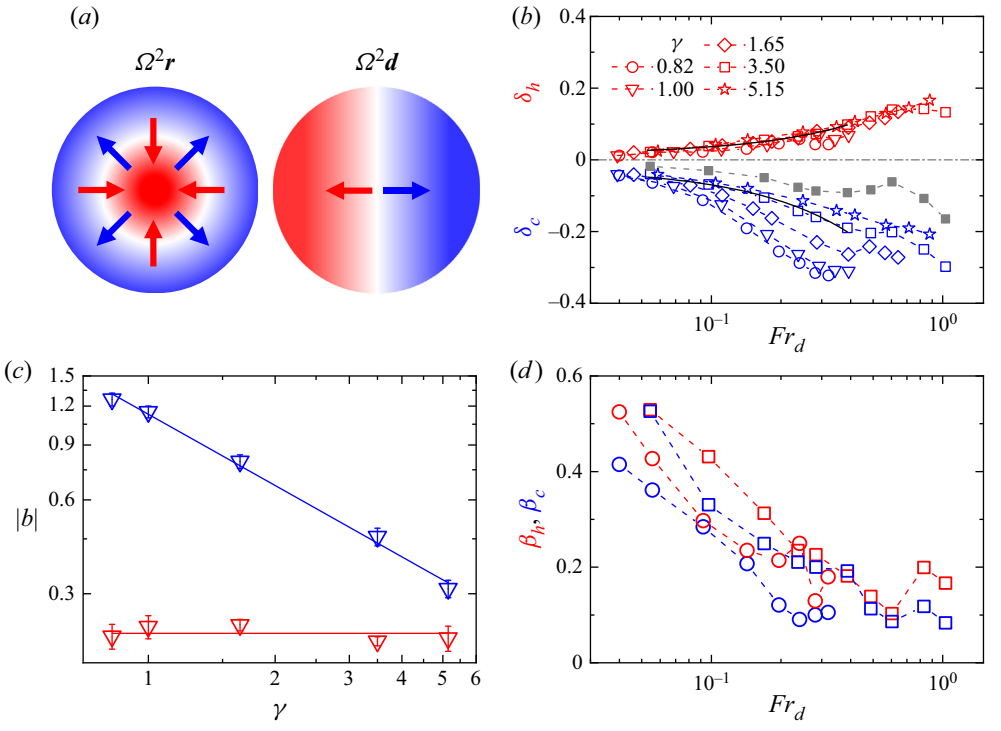

Figure 8. (*a*) A schematic sketch showing the different effects of the axisymmetrically distributed ($\Omega^2 r$) and the directed ($\Omega^2 d$) centrifugal forces. (*b*) The temperature contrast δ_h (δ_c) of the hot (cold) coherent structure as a function of Fr_d for different γ. The grey solid squares are $\delta_h + \delta_c$ for $\gamma = 3.50$. The black solid lines are linear fittings, $\delta_{h/c} = a + bFr_d$, to the temperature contrasts of $\gamma = 3.50$ in the weak-Fr_d regime. (*c*) The slope $|b|$ of the linear fitting versus γ. Red solid line indicates the average value of 0.224 for the hot coherent structures. Blue solid line represents a fitting $|b| = 1.13\gamma^{-0.76\pm0.03}$ to the blue inverted triangles. The error bars are the fitting errors. (*d*) The distribution range β_h (β_c) along the azimuthal direction of the hot (cold) coherent structure as a function of Fr_d for $\gamma = 0.82$ and 3.50. In all panels, blue and red symbols are for cold and hot coherent structures, respectively.

The effects of Fr_R are most obvious in the behaviours of the temperature contrasts δ_i of the hot ($i = h$) and cold ($i = c$) coherent structures, as shown in figure 8(*b*). A larger value of $|\delta_i|$ suggests a more coherent structure. It can be seen that for fixed γ, say $\gamma = 3.50$, the cold structure, because of the larger centrifugal force, is much more coherent than the hot one. And the difference in their coherency (the grey solid squares) is larger for larger Fr_d, since the difference $2Fr_R$ of their centrifugal forces increases when γ is fixed. The behaviours of δ_i with varying γ are also quite different for the hot and cold coherent structures. At fixed Fr_d, Fr_R is larger for smaller $\gamma = Fr_d/Fr_R$. Therefore, for smaller γ, the total centrifugal force for the cold structure $Fr_d + Fr_R$ is larger, but that for the hot one $Fr_d - Fr_R$ is smaller. That is the reason why the coherency of the cold structure is stronger for smaller γ, and for the hot one, it is weaker (figure 8*b*). Note that the difference in the hot temperature contrast δ_h for different γ is not so obvious. This may be explained as follows. The behaviours of δ_h and δ_c are more symmetric about $\delta = 0$ for larger $\gamma = Fr_d/Fr_R$, since compared with Fr_d, the effect of Fr_R becomes less significant. This can be seen clearly for the case of $\gamma = 5.15$ in figure 8(*b*). The total centrifugal force for the hot coherent structure is $Fr_d - Fr_R = Fr_d(1 - \gamma^{-1})$, which decreases with decreasing γ. Thus, as γ decreases, δ_h starts to approach its asymptotic value $\delta_h = 0$. However, as

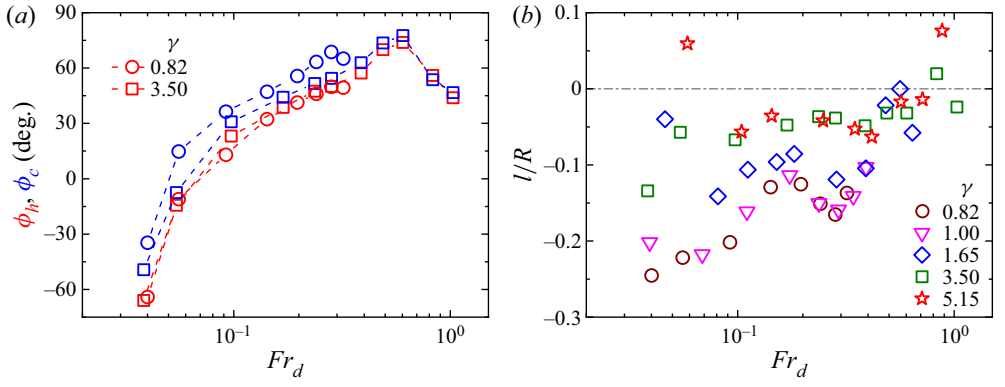

Figure 9. (*a*) The hottest (ϕ_h, red symbols) and coldest (ϕ_c, blue symbols) positions obtained from the TEE method for $\gamma = 0.82$ and 3.50. Similar behaviour can be observed for other γ, which is reflected in the behaviours of the normalized offset distance l/R in (*b*).

shown in figure 8(*b*), there is very limited space for δ_h with $\gamma < 5.15$ and the data seems to collapse together. The situation is different for the cold coherent structure, whose total centrifugal force $Fr_d + Fr_R = Fr_d(1 + \gamma^{-1})$ increases with decreasing γ. The asymptotic value of δ_c is $\delta_c = -0.5$, and the space for δ_c is large enough to distinguish themselves from each other. As described in § 3.3, the hot and cold fluid parcels are squeezed by the directed centrifugal force and then the heat content of these parcels condenses, resulting in a larger temperature contrast for larger Fr_d. It is likely that at small Fr_d, the above process is dominated by linear dynamics. Therefore, a linear function $\delta_{h/c} = a + bFr_d$ is used to describe the behaviours of δ_h and δ_c in the weak-Fr_d regime, which does not work well for the strong-Fr_d regime. The values of the slope $|b|$ are plotted in figure 8(*c*). It is a constant $b = 0.224$ for δ_h, but for δ_c, $|b|$ follows a power-law behaviour, $|b| = 1.13\gamma^{-0.76\pm0.03}$.

Figure 8(*d*) displays the distribution range β_i along the azimuthal direction of the hot ($i = h$) and cold ($i = c$) coherent structures, which implies the size of these structures. Since there are only eight thermistors in the sidewall, the azimuthal resolution may be not high enough to resolve the size of the coherent structures, especially for the large Fr_d cases. Thus, the data for different γ are scattered and no functions are tried to fit the data. But the overall trend can be identified easily, as exemplified by the data of $\gamma = 0.82$ and 3.50 in figure 8(*d*). It can be seen that, the size of the coherent structures decreases with increasing Fr_d, and overall, the cold structure is smaller than the hot one. This is because the squeezing force for the cold structure $Fr_d + Fr_R$ is larger than the hot one $Fr_d - Fr_R$.

As discussed in § 3.3, the heat transport behaviour is determined by the increased coherency and the decreased size of the coherent structures, which, as shown here, are also affected by Fr_R. The effect of $+Fr_R$ results in the cold structures having a stronger coherency and smaller physical size, but the effects are opposite for the hot structures due to the effect of $-Fr_R$. Since both hot and cold coherent structures contribute to the global heat transport, the effects of Fr_R are largely cancelled out for Nu. That is why Fr_d dominates the global features of the system, and Fr_R only has some secondary effects on the local properties.

The asymmetry between the hot and cold coherent structures can be also found from their cluster centres. Two examples for $\gamma = 0.82$ and 3.50 are plotted in figure 9(*a*), which shows that the offset of the cold cluster centre ϕ_c is larger than the hot one ϕ_h, and their difference is larger for smaller γ. This asymmetry results in an offset distance l (figure 1*b*),

which can be calculated as $l = R\langle \sin((\tilde{\phi}_h - \tilde{\phi}_c)/2)\rangle_t$, and are plotted in figure 9(*b*). It can be seen that l is negative for nearly all cases and its magnitude $|l|$ is larger for smaller γ. These results suggest that ϕ_c is always larger than ϕ_h, and their difference $|\phi_c - \phi_h|$ is larger for smaller γ. All these behaviours, as explained above, can be also attributed to the secondary effects of Fr_R.

4. Conclusions

A novel experiment was performed in RRBC, where the convection cell was shifted away from the rotation axis by a distance d. With this configuration, the centrifugal force felt by a fluid parcel can be decomposed into an axisymmetrical part $Fr_R = \Omega^2 R/g$ and a directed one $Fr_d = \Omega^2 d/g$. The global features of this system have been reported in Hu *et al.* (2021), which mainly concerns the flow properties with and without offset effects. In this paper, the local properties after the offset effects set in are investigated further, which show different features before and after $Fr_{d,max}$.

Both the local temperature fluctuations and the PSDs measured at the cell centre imply that the flow changes from a turbulent state into a laminar one at $Fr_{d,max}$. This is consistent with PIV measurements, which show that the bulk flow is full of columns at small Fr_d, and becomes 'empty' at large Fr_d. This transition, occurring at around $Fr_{d,max}$, is consistent with the regime division by the optimal heat transport state at $Fr_{d,max}$. By introducing an effective gravity $\boldsymbol{g'} = \boldsymbol{g} + \Omega^2 \boldsymbol{d}$, the emergence of these two different flow states can be understood qualitatively by an equivalent tilted RRBC system. On the other hand, the properties of the hot and cold coherent structures near the sidewall also show a transition at $Fr_{d,max}$. The vertical variations of the sidewall temperature δT_w first decrease with Fr_d, and then start to increase at $Fr_{d,max}$, which indicates that these two coherent structures are mostly uniform along the vertical direction at $Fr_{d,max}$. Their temperature contrasts show a linear dependence on Fr_d and start to deviate from this linear behaviour when $Fr_d > Fr_{d,max}$. These results can be summarized by the $Fr_d - \gamma$ phase space shown in figure 10, which is divided into three regimes by $Fr_{d,c}$ and $Fr_{d,max}$. In the first regime with $Fr_d < Fr_{d,c}$, the flow dynamics in the off-centred system is similar to the centred one. In the weak-Fr_d regime with $Fr_{d,c} < Fr_d < Fr_{d,max}$, the hot and cold coherent structures near the sidewall start to emerge and the bulk is still full of hot and cold columns, whose motion along the direction of d is enhanced. But in the strong-Fr_d regime with $Fr_d > Fr_{d,max}$, the columns are moving out of the bulk and merge with those near the sidewall, resulting in an 'empty' bulk and much stronger coherent structures near the sidewall.

Besides the dominant effects of Fr_d, the secondary effects of Fr_R are also investigated. Detailed analysis of the hot and cold coherent structures reveals that their local properties are not symmetric. This is because, for the cold structure, Fr_R cooperates with Fr_d, but these two forces compete with each other for the hot one. Thus, compared with the hot coherent structure, the cold one is more coherent but with a smaller size. The offset of the cold cluster centre from the farthest point ϕ_c is also larger than the hot one ϕ_h, resulting in an offset distance l, whose magnitude is larger for smaller γ. Although the respective properties of the hot and cold coherent structures are affected by Fr_R, its effects on global features are largely cancelled out.

The present results may have some implications for the tidal effects in astrophysics. In a two-body system, such as the Jupiter–Io system, besides the familiar gravitational pull between two mass centres, each body experiences an additional force arising from the non-spherical part of the mass distribution, namely, the tidal force. This force can be conveniently expanded in terms of spherical functions (e.g. Zahn 1977). But as an

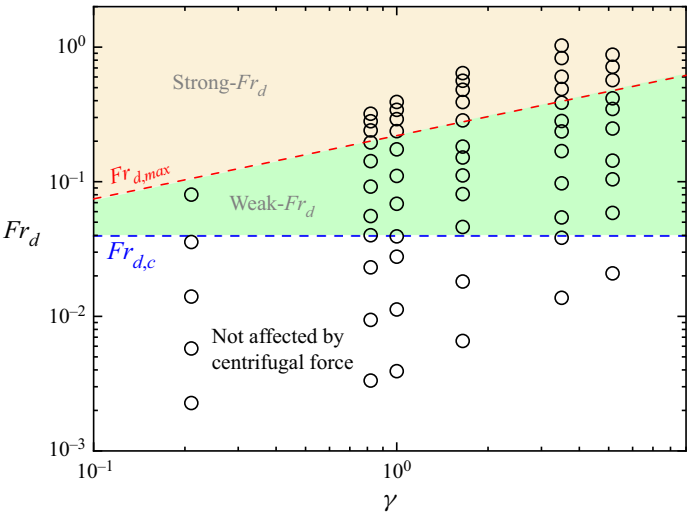

Figure 10. The phase space $Fr_d - \gamma$, which is divided into three regimes by the blue dash line $Fr_{d,c} = 0.04$ and the red dash line $Fr_{d,max} = 0.22\gamma^{0.47}$. The white area is the regime where the effect of Fr_d does not set in. The green- and yellow-shaded areas are the weak-Fr_d and strong-Fr_d regimes, respectively. The open circles are the cases covered by the present experiment.

estimation, let us consider the subjovian and antijovian points on Io, where the tidal forces are most significant, with magnitudes of

$$F_{tidal}^{sub} = \frac{GM_J}{R^2}\left(\frac{1}{(1-\epsilon)^2} - 1\right) \quad \text{and} \quad F_{tidal}^{anti} = \frac{GM_J}{R^2}\left|\frac{1}{(1+\epsilon)^2} - 1\right|, \tag{4.1a,b}$$

respectively. Here, G is the gravitational constant, M_J is the mass of Jupiter, and $\epsilon = r/R < 1$ is the ratio of Io's radius r to its orbital radius R. After a simple Taylor expansion, we can obtain $F_{tidal}^{sub} = F_0 + F_1 + \cdots$ and $F_{tidal}^{anti} = F_0 - F_1 + \cdots$, where $F_0 = 2GM_J\epsilon/R^2$ and $F_1 = 3GM_J\epsilon^2/R^2$. Now, it is straightforward that the directed centrifugal force Fr_d, that condenses the hot (cold) fluid parcels near the left-hand (right-hand) sidewall, resembles the main component of the tidal force F_0, which clusters the volcanoes near the subjovian and antijovian points on Io; and the force $+Fr_R$ $(-Fr_R)$ acting on cold (hot) fluid parcels plays a similar role to the secondary term $+F_1$ $(-F_1)$ near the subjovian (antijovian) point. In the Jupiter–Io system, $\epsilon \ll 1$, and the effect of $F_1(\propto \epsilon^2)$ may not be observable. But in a close binary star system (Zahn & Bouchet 1989), where two nearly identical stars orbit around their mass centre and ϵ is not too small, the effect of F_1 may be observable. Therefore, broadly speaking, our off-centred system can serve as an excellent laboratory model to study the tidal effects.

Funding. This work was supported by the National Natural Science Foundation of China (NSFC) (grant nos. 12072144 and 12232010) and the Research Grants Council of Hong Kong SAR (grant nos. N_CUHK437/15 and CUHK14302317).

Declaration of interests. The authors report no conflict of interest.

Author ORCIDs.
Yun-Bing Hu https://orcid.org/0000-0002-2319-275X;
Ke-Qing Xia https://orcid.org/0000-0001-5093-9014.

References

Ahlers, G., Grossmann, S. & Lohse, D. 2009 Heat transfer and large scale dynamics in turbulent Rayleigh–Bénard convection. *Rev. Mod. Phys.* **81**, 503–537.

Brown, E. & Ahlers, G. 2006 Rotations and cessations of the large-scale circulation in turbulent Rayleigh–Bénard convection. *J. Fluid Mech.* **568**, 351–386.

Brown, E., Nikolaenko, A. & Ahlers, G. 2005 Reorientation of the large-scale circulation in turbulent Rayleigh–Bénard convection. *Phys. Rev. Lett.* **95**, 084503.

Chandrasekhar, S. 1981 *Hydrodynamic and Hydromagnetic Stability*. Courier Corporation.

Cheng, J.S., Madonia, M., Aguirre, G., Andrés, J. & Kunnen, R.P.J. 2020 Laboratory exploration of heat transfer regimes in rapidly rotating turbulent convection. *Phys. Rev. Fluids* **5**, 113501.

Chong, K.-L., Shi, J.-Q., Ding, G.-Y., Ding, S.-S., Lu, H.-Y., Zhong, J.-Q. & Xia, K.-Q. 2020 Vortices as Brownian particles in turbulent flows. *Sci. Adv.* **6**, eaaz1110.

Ding, S.-S., Chong, K.-L., Shi, J.-Q., Ding, G.-Y., Lu, H.-Y., Xia, K.-Q. & Zhong, J.-Q. 2021 Inverse centrifugal effect induced by collective motion of vortices in rotating thermal convection. *Nat. Commun.* **12**, 5585.

Ecke, R.E. & Shishkina, O. 2023 Turbulent rotating Rayleigh–Bénard convection. *Annu. Rev. Fluid Mech.* **55** (1), 603–638.

Grooms, I., Julien, K., Weiss, J.B. & Knobloch, E. 2010 Model of convective taylor columns in rotating Rayleigh–Bénard convection. *Phys. Rev. Lett.* **104**, 224501.

Hamilton, C.W., Beggan, C.D., Still, S., Beuthe, M., Lopes, R.M.C., Williams, D.A., Radebaugh, J. & Wright, W. 2013 Spatial distribution of volcanoes Io: implications for tidal heating and magma ascent. *Earth Planet. Sci. Lett.* **361**, 272–286.

von Hardenberg, J., Goluskin, D., Provenzale, A. & Spiegel, E.A. 2015 Generation of large-scale winds in horizontally anisotropic convection. *Phys. Rev. Lett.* **115**, 134501.

Horn, S. & Aurnou, J.M. 2018 Regimes of coriolis-centrifugal convection. *Phys. Rev. Lett.* **120**, 204502.

Horn, S. & Aurnou, J.M. 2019 Rotating convection with centrifugal buoyancy: numerical predictions for laboratory experiments. *Phys. Rev. Fluids* **4**, 073501.

Hu, Y.-B., Huang, S.-D., Xie, Y.-C. & Xia, K.-Q. 2021 Centrifugal-force-induced flow bifurcations in turbulent thermal convection. *Phys. Rev. Lett.* **127**, 244501.

Hu, Y.-B., Xie, Y.-C. & Xia, K.-Q. 2022 On the centrifugal effect in turbulent rotating thermal convection: onset and heat transport. *J. Fluid Mech.* **938**, R1.

Julien, K., Rubio, A.M., Grooms, I. & Knobloch, E. 2012 Statistical and physical balances in low Rossby number Rayleigh–Bénard convection. *Geophys. Astrophys. Fluid Dyn.* **106**, 392–428.

King, E.M., Stellmach, S., Noir, J., Hansen, U. & Aurnou, J.M. 2009 Boundary layer control of rotating convection systems. *Nature* **457**, 301–304.

Kunnen, R.P.J. 2021 The geostrophic regime of rapidly rotating turbulent convection. *J. Turbul.* **22**, 267–296.

Kunnen, R.P.J., Geurts, B.J. & Clercx, H.J.H. 2010 Experimental and numerical investigation of turbulent convection in a rotating cylinder. *J. Fluid Mech.* **642**, 445–476.

Kunnen, R.P.J., Stevens, R.J.A.M., Overkamp, J., Sun, C., van Heijst, G.F. & Clercx, H.J.H. 2011*a* The role of Stewartson and Ekman layers in turbulent rotating Rayleigh–Bénard convection. *J. Fluid Mech.* **688**, 422–442.

Kunnen, R.P.J., Stevens, R.J.A.M., Overkamp, J., Sun, C., van Heijst, G.F. & Clercx, H.J.H. 2011*b* The role of Stewartson and Ekman layers in turbulent rotating Rayleigh–Bénard convection. *J. Fluid Mech.* **688**, 422–442.

Noto, D., Tasaka, Y., Yanagisawa, T. & Murai, Y. 2019 Horizontal diffusive motion of columnar vortices in rotating Rayleigh–Bénard convection. *J. Fluid Mech.* **871**, 401–426.

Novi, L., von Hardenberg, J., Hughes, D.W., Provenzale, A. & Spiegel, E.A. 2019 Rapidly rotating Rayleigh–Bénard convection with a tilted axis. *Phys. Rev.* E **99**, 053116.

Plumley, M., Julien, K., Marti, P. & Stellmach, S. 2016 The effects of Ekman pumping on quasi-geostrophic Rayleigh–Bénard convection. *J. Fluid Mech.* **803**, 51–71.

Proudman, J. 1916 On the motion of solids in a liquid possessing vorticity. *Proc. R. Soc.* A **92**, 408–424.

Segatz, M., Spohn, T., Ross, M.N. & Schubert, G. 1988 Tidal dissipation, surface heat flow, and figure of viscoelastic models of Io. *Icarus* **75**, 187–206.

Spencer, J.R. & Schneider, N.M. 1996 Io on the eve of Galileo mission. *Annu. Rev. Earth Planet. Sci.* **24**, 125–190.

Sprague, M., Julien, K., Knobloch, E. & Werne, J. 2006 Numerical simulation of an asymptotically reduced system for rotationally constrained convection. *J. Fluid Mech.* **551**, 141–174.

Steinke, T., van Sliedregt, D., Vilella, K., van der Wal, W. & Vermeersen, B. 2020 Can a combination of convective and magmatic heat transport in the mantle explain Io's volcanic pattern? *J. Geophys. Res.* **125**, e2020JE006521.

STEVENS, R.J.A.M., CLERCX, H.J.H. & LOHSE, D. 2010 Optimal Prandtl number for heat transfer in rotating Rayleigh–Bénard convection. *New J. Phys.* **12**, 075005.

STEVENS, R.J.A.M., CLERCX, H.J.H. & LOHSE, D. 2013 Heat transport and flow structure in rotating Rayleigh–Bénard convection. *Eur. J. Mech. B/Fluids* **40**, 41–49.

SUN, C., XIA, K.-Q. & TONG, P. 2005 Three-dimensional flow structures and dynamics of turbulent thermal convection in a cylindrical cell. *Phys. Rev.* E **72**, 026302.

TAYLOR, G.I. 1923 Experiments on the motion of solid bodies in rotating fluids. *Proc. R. Soc.* A **104**, 213–218.

TYLER, R.H., HENNING, W.G. & HAMILTON, C.W. 2015 Tidal heating in a magma ocean within Jupiter's Moon Io. *Astrophys. J. Suppl. S.* **218**, 22.

WEISS, S., STEVENS, R.J.A.M., ZHONG, J.-Q., CLERCX, H.J.H., LOHSE, D. & AHLERS, G. 2010 Finite-size effects lead to supercritical bifurcations in turbulent rotating Rayleigh–Bénard convection. *Phys. Rev. Lett.* **105**, 224501.

WEISS, S., WEI, P. & AHLERS, G. 2016 Heat-transport enhancement in rotating turbulent Rayleigh–Bénard convection. *Phys. Rev.* E **93**, 043102.

XI, H.-D. & XIA, K.-Q. 2007 Cessations and reversals of the large-scale circulation in turbulent thermal convection. *Phys. Rev.* E **75**, 066307.

XI, H.-D., ZHOU, S.-Q., ZHOU, Q., CHAN, T.-S. & XIA, K.-Q. 2009 Origin of the temperature oscillation in turbulent thermal convection. *Phys. Rev. Lett.* **102**, 044503.

XIA, K.-Q., SUN, C. & ZHOU, S.-Q. 2003 Particle image velocimetry measurement of the velocity field in turbulent thermal convection. *Phys. Rev.* E **68**, 066303.

ZAHN, J.P. 1977 Tidal friction in close binary stars. *Astron. Astrophys.* **57**, 383–394.

ZAHN, J.P. & BOUCHET, L. 1989 Tidal evolution of close binary stars. II. Orbital circularization of late-type binaries. *Astron. Astrophys.* **223**, 112–118.

ZHANG, L., DING, G.-Y. & XIA, K.-Q. 2021 On the effective horizontal buoyancy in turbulent thermal convection generated by cell tilting. *J. Fluid Mech.* **914**, A15.

ZHONG, J.-Q. & AHLERS, G. 2010 Heat transport and the large-scale circulation in rotating turbulent Rayleigh–Bénard convection. *J. Fluid Mech.* **665**, 300–333.

ZHONG, J.-Q., STEVENS, R.J.A.M., CLERCX, H.J.H., VERZICCO, R., LOHSE, D. & AHLERS, G. 2009 Prandtl-, Rayleigh-, and Rossby-number dependence of heat transport in turbulent rotating Rayleigh–Bénard convection. *Phys. Rev. Lett.* **102**, 044502.

ZHOU, Q., XI, H.-D., ZHOU, S.-Q., SUN, C. & XIA, K.-Q. 2009 Oscillations of the large-scale circulation in turbulent Rayleigh–Bénard convection: the sloshing mode and its relationship with the torsional mode. *J. Fluid Mech.* **630**, 367–390.

ZHOU, Q. & XIA, K.-Q. 2013 Thermal boundary layer structure in turbulent Rayleigh–Bénard convection in a rectangular cell. *J. Fluid Mech.* **721**, 199–224.